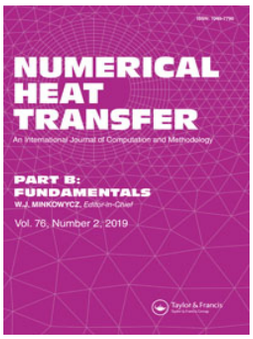

Taylor & Francis
Taylor & Francis Group

Numerical Heat Transfer, Part B: Fundamentals
An International Journal of Computation and Methodology

ISSN: 1040-7790 (Print) 1521-0626 (Online) Journal homepage: www.tandfonline.com/journals/unhb20

The characteristic boundary condition in pressure-based methods

F. Moukalled, L. Mangani & M. Darwish

To cite this article: F. Moukalled, L. Mangani & M. Darwish (2019) The characteristic boundary condition in pressure-based methods, Numerical Heat Transfer, Part B: Fundamentals, 76:2, 43-59, DOI: 10.1080/10407790.2019.1644942

To link to this article: https://doi.org/10.1080/10407790.2019.1644942

NUMERICAL HEAT TRANSFER, PART B: FUNDAMENTALS
2019, VOL. 76, NO. 2, 43–59
https://doi.org/10.1080/10407790.2019.1644942

Taylor & Francis
Taylor & Francis Group

The characteristic boundary condition in pressure-based methods

F. Moukalled[a], L. Mangani[b], and M. Darwish[a]

[a]Mechanical Engineering Department, American University of Beirut, Beirut, Lebanon; [b]Hochschule Luzern, Technik und Architektur, Horw, Switzerland

ABSTRACT

This article deals with the implementation of the characteristic boundary condition, also known as the pressure far field boundary condition, in segregated pressure-based flow solvers. This boundary condition applies the Riemann invariants to determine the flow variables at domain inlets and outlets. The newly developed method is implemented in a cell-centered unstructured grid code following a finite volume discretization. Testing is performed by solving the following problems: turbulent flow over a flat plate; inviscid transonic flow over a circular are bump; inviscid supersonic flow over three equidistant circular arc bumps; turbulent flow over an axisymmetric transonic bump; turbulent flow over a NACA 0012 airfoil at 10° angle of attack; and turbulent flow over the three-dimensional ONERA M6 wing at 3.06° angle of attack. Predictions with the current pressure-based solver are compared with similar ones generated using a density-based method and with experimental data. Results are in excellent agreement.

ARTICLE HISTORY
Received 3 March 2019
Accepted 12 July 2019

1. Introduction

Numerical techniques for solving the Navier-stokes equations are well developed and methods such as the Finite Volume Method (FVM) and Finite Element Method are capable of predicting flows in complex geometries. The implementation of these methods followed two routes denoted in the literature by the density-based and pressure-based approaches.

The density-based approach [1–5] was originally developed to solve compressible flow problems, and then extended through the pseudo or artificial compressibility technique [6, 7] to handle incompressible flows. To overcome the decrease in the convergence rate and ensure convergence over all speed ranges, preconditioning of the stiff matrices was introduced and several methods [8–12] following this approach have been developed.

On the other hand, the pressure based method [13–24] was originally developed for the solution of incompressible flow problems, and then extended to handle compressible flow problems [19–24] allowing solutions to be obtained over the entire flow spectrum from low subsonic to hypersonic including transonic flows. This article follows the pressure-based approach.

These methods generate numerical solutions by solving the set of conservation equations subject to prescribed boundary conditions. Depending on the physical situation, different boundary conditions are encountered [25, 26]. In a recent article [27] the authors have described the implementation, within a pressure-based solver, of several boundary conditions for both incompressible and compressible flows. An interesting boundary condition that was not covered in [27] is the pressure far field boundary condition. This boundary condition is also known as the characteristic

CONTACT F. Moukalled fmukalled@aub.edu.lb Mechanical Engineering Department, American University of Beirut, Riad El-Solh, Beirut 1107 2020, Lebanon.
Color versions of one or more of the figures in the article can be found online at www.tandfonline.com/unhb.

Nomenclature

c	speed of sound; also chord length	T	temperature
c_p	specific heat at constant pressure	U	velocity component normal to boundary
d	normal distance to the nearest wall	$\mathbf{v}$	velocity vector
$\mathbf{D}$	tensor operator	***Greek symbols***	
$\mathcal{D}$	scalar in Eq. (17)	ϕ	general scalar variableμdynamic viscosity
$\mathbf{f}_b$	body force per unit volume	μ_t	turbulent viscosity
$\mathbf{I}$	identity matrix	$\tilde{\nu}$	kinematic eddy viscosity
M	Mach number	γ	specific heat ratio
$\dot{m}$	mass flow rate	Γ^{ϕ}	diffusion coefficient in general equation
$\mathbf{n}$	outward normal unit vector	ρ	fluid density τ deviatoric stress tensor
p	pressure	***Subscripts***	
Pr	laminar Prandtl number	b	refers to boundary
Pr_t	turbulent Prandtl number	C	refers to main grid point
p'	pressure correction	∞	refers to free stream
$\dot{q}_V$	heat generation per unit volume	***Superscripts***	
Q^{ϕ}	source term in general equation	$\mathbf{v}$	refers to velocity
R	gas constant	T	refers to the transpose of a vector
$R^{-}(R^{+})$	Riemann invariant corresponding to incoming (outgoing) characteristic waves	n	refers to value at the previous iteration
		$\bar{}$	refers to an interpolated value
$\mathbf{S}$	surface vector	$*$	refers to an updated value during an iteration
S	magnitude of $\mathbf{S}$	$'$	refers to correction
s_b	entropy at inflow/outflow		
t	time		

boundary condition because it applies the Riemann invariants, which correspond to incoming and outgoing characteristics waves, to determine the flow variables at the boundaries. Even though this boundary condition is well developed and accurately described for density-based methods [28–30], its implementation in pressure-based solvers is still not well documented in the literature. Except for the article by Mathur and Murthy [31], the authors were not able to find any work describing its derivation and implementation in a pressure-based solver. It is the objective of this work to perform this task.

The article is organized as follows: First, the set of conservation equations governing compressible flow is reviewed. Then the algebraic equations resulting from discretizing the conservation equations in the context of the FVM are briefly presented. This is followed by a detailed analysis of the far field Riemann invariant boundary condition and its implementation in a pressure based solver. Finally, the new technique is implemented in an unstructured grid, pressure-based, Finite Volume flow solver and used to solve for a number of inviscid and turbulent compressible subsonic, transonic, and supersonic test cases.

2. The governing equations

The prediction of turbulent compressible flows necessitates solving the continuity, momentum, energy, and turbulence model equations. Adopting the Spalart-Allmaras one equation turbulence model [32–34], these equations are given, respectively, by

$$\frac{\partial \rho}{\partial t} + \nabla \cdot (\rho \mathbf{v}) = 0 \tag{1}$$

$$\frac{\partial}{\partial t}[\rho \mathbf{v}] + \nabla \cdot \{\rho \mathbf{v}\mathbf{v}\} = -\nabla p + [\nabla \cdot \tau] + \mathbf{f}_b \tag{2}$$

$$\frac{\partial}{\partial t}\left(\rho c_p T\right) + \nabla \cdot \left[\rho c_p \mathbf{v} T\right] = \nabla \cdot \left[\left(\frac{\mu c_p}{Pr} + \frac{\mu_t c_p}{Pr_t}\right)\nabla T\right] + \rho T \frac{Dc_p}{Dt} + \frac{Dp}{Dt} + \tau : \nabla \mathbf{v} + \dot{q}_V \tag{3}$$

$$\frac{\partial}{\partial t}(\rho\tilde{\nu}) + \nabla\cdot[\rho\mathbf{v}\tilde{\nu}] = \nabla\cdot\left[\left(\frac{\mu+\rho\tilde{\nu}}{\sigma}\right)\nabla\tilde{\nu}\right] + \rho C_{b1}(1-f_{t2})\tilde{S}\tilde{\nu} - \left[\rho C_{w1}f_w - \rho\frac{C_{b1}}{\kappa^2}f_{t2}\right]\left(\frac{\tilde{\nu}}{d}\right)^2 + \rho\frac{C_{b2}}{\sigma}(\nabla\tilde{\nu})^2 \tag{4}$$

where $\mathbf{v}$, p, T, $\tilde{\nu}$, ρ, $\mathbf{f}_b$, c_p, μ, and $\dot{q}_V$ represent the velocity vector, pressure, temperature, kinematic eddy viscosity, density, body force per unit volume, specific heat at constant pressure, dynamic viscosity, and heat generation per unit volume, respectively. In addition, τ represents the stress tensor, which, using the Boussinesq assumption is expressed as

$$\boldsymbol{\tau} = (\mu+\mu_t)\left\{\nabla\mathbf{v} + (\nabla\mathbf{v})^{\mathrm{T}}\right\} - \frac{2}{3}(\mu+\mu_t)(\nabla\cdot\mathbf{v})\mathbf{I} - \frac{2}{3}\rho k\mathbf{I} \tag{5}$$

where k is the turbulence kinetic energy and the expressions for the calculation of the various terms in Eq. (4) in addition to the turbulent viscosity and model constants can be found in [32–34]. Because the turbulent kinetic energy is not readily available when using the Spalart-Allmaras turbulence model, its contribution to the shear stress is neglected in Eq. (5). Moreover, for compressible flow, an equation of state relating density to temperature and pressure is required. For an ideal gas this equation is given by

$$\rho = \frac{p}{RT} \tag{6}$$

where R is the gas constant.

3. The discretized equations

If ϕ denotes a scalar variable, then the conservation Eqs. (1)–(4) can be written in the following general form:

$$\underbrace{\frac{\partial}{\partial t}(\rho\phi)}_{transient-term} + \underbrace{\nabla\cdot[\rho\mathbf{v}\phi]}_{convection-term} = \underbrace{\nabla\cdot[\Gamma^{\phi}\nabla\phi]}_{diffusion-term} + \underbrace{Q^{\phi}}_{source-term} \tag{7}$$

where the expressions for Γ^{ϕ} and Q^{ϕ} can be deduced from the parent equation. Therefore, the discretization of the mass, momentum, energy, or kinematic eddy viscosity equation reduces to the discretization of the general conservation Eq. (7). Since the work adopts a finite volume method, the first step is to subdivide the computational domain into a number of non-overlapping cells, each associated with a grid point placed at its centroid (Figure 1*a*). The second step produces a semi-discretized form of the conservation equation by integrating the equation over an element and transforming the volume integrals of the convection and diffusion fluxes into surface integrals with the aid of the divergence theorem. In a final step, profiles approximating the variation of ϕ between cell centroids yields the final algebraic form of the equation.

The discretization of the diffusion flux follows a semi-implicit scheme [35–40] that splits the flux into two parts. The first part is treated implicitly, while the second part is evaluated explicitly and added as a source in a deferred correction manner. For the discretization of the convection flux, the second order minmod scheme [41] is adopted and applied in the context of the NVF methodology [41] following the deferred correction approach of Khosla and Rubin [42]. The discretization of the transient term follows either a first or a second order temporal scheme [43]. Finally, the method evaluates the remaining terms explicitly by assuming their values at the cell centroid to be equal to their mean values over the whole element. This yields an algebraic equation that represents the numerical equivalent of the original conservation equation. Details on this procedure can be found in the literature (e.g. [16, 19]). A

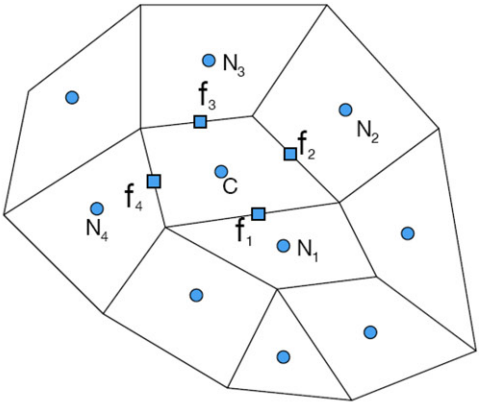

(a)

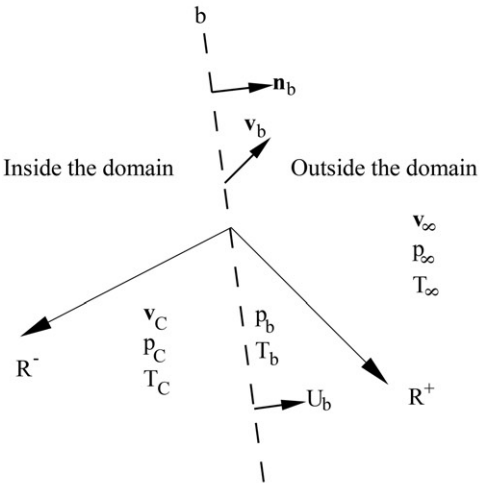

(b)

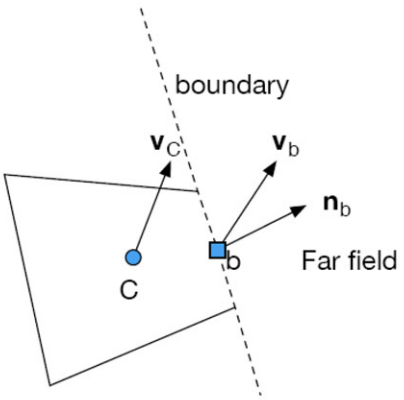

(c)

Figure 1. (a) Domain discretization into a number of elements; (b) characteristics at a boundary; (c) a boundary element.

similar equation results in every element with their collection forming an algebraic system that is solved iteratively, subject to boundary conditions described next, until a converged solution is obtained.

To evaluate the pressure field, a pressure correction p' ($p' = p - p^*$, where p^* is the solution from the previous iteration) is defined and a pressure correction equation is derived by combining the discretized momentum and continuity equations as in the SIMPLE procedure of Patankar [13, 16, 19].

Since a collocated grid is used, checkerboard pressure and velocity fields are suppressed through the use of the Rhie-Chow interpolation technique [19, 44] according to which the velocity at cell faces is computed as

$$\mathbf{v}_f = \overline{\mathbf{v}_f} - \overline{\mathbf{D}_f^{\mathbf{v}}}\left(\nabla p_f - \overline{\nabla p_f}\right) \tag{8}$$

In Eq. (8), the bar indicates a value obtained by interpolation.

4. Pressure far field boundary condition

To close the system of algebraic equations, boundary conditions are required. Many of the encountered boundary conditions were discussed in [27]. The focus here is on the implementation in a pressure-based solver of the pressure far field boundary condition that was not covered in [27]. This boundary condition is known also as the characteristic boundary condition because it applies the Riemann invariants, which correspond to incoming and outgoing characteristics waves, to determine the flow variables at the boundaries. It is applicable to both subsonic and supersonic flows at domain inlets and outlets. This boundary condition requires the complete specification of the free-stream conditions in terms of velocity, pressure, and temperature and is applicable when the density is calculated using the ideal gas equation of state.

4.1. Pressure far field equations

The Riemann invariants corresponding to the incoming (R^-) and outgoing (R^+) characteristic waves, schematically depicted in Figure 1b, are given by

$$R^+ = U_C + \frac{2c_C}{\gamma - 1} \quad R^- = U_\infty - \frac{2c_\infty}{\gamma - 1} \tag{9}$$

In the above equation and the equations to follow, subscripts c, ∞, and b represent conditions at the first interior grid point (c), in the free-stream (∞), and along the boundary (b). Moreover, U represents the component of the velocity vector normal to the boundary. Denoting the outward unit surface vector at the boundary by $\mathbf{n}_b$, this normal velocity component can be expressed as

$$U = \mathbf{v} \cdot \mathbf{n}_b \tag{10}$$

In addition, c represents the speed of sound computed as

$$c = \sqrt{\frac{\gamma p}{\rho}} = \sqrt{\gamma R T} \tag{11}$$

The normal component of velocity and speed of sound at the boundary are computed from the Riemann invariants as

$$U_b = \mathbf{v}_b \cdot \mathbf{n}_b = \frac{1}{2}(R^+ + R^-) \quad c_b = \frac{\gamma - 1}{4}(R^+ - R^-) \tag{12}$$

Substitution of Eq. (9) in Eq. (12) leads to the following expressions for U_b and c_b :

$$U_b = \frac{1}{2}(U_c + U_\infty) - \frac{1}{\gamma - 1}(c_\infty - c_C) \quad c_b = -\frac{\gamma - 1}{4}(U_\infty - U_c) + \frac{1}{2}(c_\infty + c_C) \tag{13}$$

Assuming an ideal gas flow, the boundary entropy, density, and pressure at inlets and outlets are computed as

$$s_b = \begin{cases} \dfrac{c_C^2}{\gamma \rho_c^{\gamma-1}} & outflow \\ \dfrac{c_\infty^2}{\gamma \rho_\infty^{\gamma-1}} & inflow \end{cases} \qquad \rho_b = \left(\frac{c_b^2}{\gamma s_b}\right)^{1/(\gamma-1)} \qquad p_b = \frac{\rho_b c_b^2}{\gamma} \tag{14}$$

4.2. Implementation of pressure far field in segregated pressure-based solvers

Implementation of this boundary condition in a segregated pressure-based solver requires deriving an equation for boundary pressure correction from which the pressure p_b, density ρ_b, velocity $\mathbf{v}_b$, and mass flow rate $\dot{m}_b$ can be calculated. This allows the calculation of the pressure gradient and convective fluxes while the shear stress τ_b is set to zero since the flow is assumed locally inviscid.

In a segregated pressure-based algorithm, a better estimate to the value of any variable ϕ ($\phi = p, U, \mathbf{v}, \dot{m}, \rho$) is assumed to be obtained by adding a correction denoted by ϕ' to an existing estimate ϕ^* such that

$$\phi = \phi^* + \phi' \tag{15}$$

where the superscript $*$ refers to the latest available value during an iteration. Along a boundary face (Figure 1*c*), the mass flow rate can be expressed as

$$\dot{m}_b = \dot{m}_b^* + \dot{m}_b' = \left(\rho_b^* + \rho'_b\right)\left(U_b^* + U_b'\right)S_b \approx \rho_b^* U_b^* S_b + \rho_b^* U_b' S_b + \rho'_b U_b^* S_b \tag{16}$$

Through the use of the Rhie-Chow interpolation (Eq. (8)), the velocity correction at the boundary face can be written as

$$\mathbf{v}_b' = -\mathbf{D}_C \nabla p_b' \Rightarrow U_b' S_b = -\mathbf{D}_C \nabla p_b' \cdot \mathbf{S}_b \Rightarrow U_b' S_b \approx -D_C\left(p_b' - p_C'\right) \tag{17}$$

where boundary face average is written in terms of the element value [19, 27]. Moreover, transforming Eq. (13) into an equation relating correction values yields

$$\left.\begin{aligned} U_b &= \frac{1}{2}(U_c + U_\infty) - \frac{1}{\gamma - 1}(c_\infty - c_C) \Rightarrow U_b' = \frac{1}{2}U_c' + \frac{1}{\gamma - 1}c_C' \\ c_b &= -\frac{\gamma - 1}{4}(U_\infty - U_c) + \frac{1}{2}(c_\infty + c_C) \Rightarrow c_b' = \frac{\gamma - 1}{4}U_c' + \frac{1}{2}c_C' \end{aligned}\right\} \Rightarrow c_b' = \frac{\gamma - 1}{2}U_b' \tag{18}$$

Differentiating pressure with respect to density and density with respect to speed of sound leads to

$$\begin{aligned} p_b &= \frac{\rho_b c_b^2}{\gamma} \Rightarrow \frac{\partial p_b}{\partial \rho_b} = \frac{c_b^2}{\gamma} \\ \rho_b &= \left(\frac{c_b^2}{\gamma s_b}\right)^{1/(\gamma-1)} \Rightarrow \frac{\partial \rho_b}{\partial c_b} = \frac{1}{\gamma - 1}\left(\frac{c_b^2}{\gamma s_b}\right)^{-1+1/(\gamma-1)} \frac{2c_b}{\gamma s_b} = \frac{2}{\gamma - 1}\left(\frac{c_b^2}{\gamma s_b}\right)^{1/(\gamma-1)} \frac{1}{c_b} \end{aligned} \tag{19}$$

From a truncated Taylor series expansion, density and pressure corrections can be expressed as

$$\rho'_b = \frac{\partial \rho_b}{\partial c_b} c'_b \Rightarrow \rho'_b = \frac{2}{\gamma - 1}\left(\frac{c_b^2}{\gamma s_b}\right)^{1/(\gamma-1)} \frac{1}{c_b} c'_b = \frac{1}{c_b}\left(\frac{c_b^2}{\gamma s_b}\right)^{1/(\gamma-1)} U'_b \tag{20}$$

$$p'_b = \frac{\partial p_b}{\partial \rho_b} \rho'_b = \frac{c_b}{\gamma}\left(\frac{c_b^2}{\gamma s_b}\right)^{1/(\gamma-1)} U'_b = \frac{s_b}{c_b}\left(\frac{c_b^2}{\gamma s_b}\right)^{\gamma/(\gamma-1)} U'_b \tag{21}$$

Substituting Eq. (21) into Eq. (17) yields

$$U'_b S_b = -\mathcal{D}_C\left(\frac{s_b}{c_b}\left(\frac{c_b^2}{\gamma s_b}\right)^{\gamma/(\gamma-1)} U'_b - p'_C\right) \Rightarrow U'_b = \frac{\mathcal{D}_C}{S_b + \mathcal{D}_C \frac{s_b}{c_b}\left(\frac{c_b^2}{\gamma s_b}\right)^{\gamma/(\gamma-1)}} p'_C \tag{22}$$

Using Eq. (22) leads to the following expressions for the pressure and mass flow rate corrections, in terms of pressure correction, at a boundary face centroid:

$$p'_b = \frac{\frac{p_b}{c_b}\mathcal{D}_C}{S_b + \frac{p_b}{c_b}\mathcal{D}_C} p'_C \tag{23}$$

$$\dot{m}'_b = \rho^*_b U'_b S_b + \rho'_b U^*_b S_b = \frac{\rho^*_b D_C S_b}{S_b + \frac{p_b}{c_b} D_C}\left(1 + \frac{U^*_b}{c_b}\right) p'_C \tag{24}$$

Following the procedure described in [27], Eq. (24) allows modifying the coefficients of the pressure correction equation along the boundary face. After solving the pressure correction equation, the boundary values of pressure, density, velocity, temperature, and mass flow rate are updated to satisfy mass conservation. These values are used in solving the momentum and energy equations as specified velocity and static temperature boundary conditions.

5. Results and discussion

Several test cases involving the pressure far field boundary condition are considered. When available, results are compared with similar ones obtained using a density-based method and reported on the Langely research center website [45]. For these cases, the grid of average size posted on the website is used. Results obtained using these grid systems are compared with those reported on the website using the densest grid. Moreover, the one-equation Spalarat-Allmaras turbulence model is adopted for solving the turbulent flow cases.

5.1. Case 1: Turbulent flow over a flat plate with zero pressure gradient

The first problem deals with predicting the turbulent flow over a flat plate. Figure 2*a* depicts a schematic of the physical situation and boundary conditions used. Along the upper horizontal boundary, which is at a distance of 1 m away from the wall, the pressure far field boundary condition is applied. The plate length is 2 m and the domain inlet is set 1/3 m upstream of the plate. The problem is solved for a free-stream Mach number M_∞, temperature T_∞, and mid-plate Reynolds number with values of 0.2, 300 K, and 5×10^6, respectively. As shown in Figure 2*b*, a non-uniform grid system is used with denser clustering in the boundary layer and at the plate leading edge.

Results generated are reported in Figures 2*c*–2*f*. The variation of the skin friction coefficient (c_f) over the plate is displayed in Figure 2*c*. As shown, the computed profile falls on top of the one reported in [44] and obtained using a density-based method. In addition, c_f values are very close to measured data reported by Weighardt [46]. The predicted u^+ versus y^+ profile is displayed in Figure 2*d* and compared with similar theoretical ones in the log-layer and viscous-

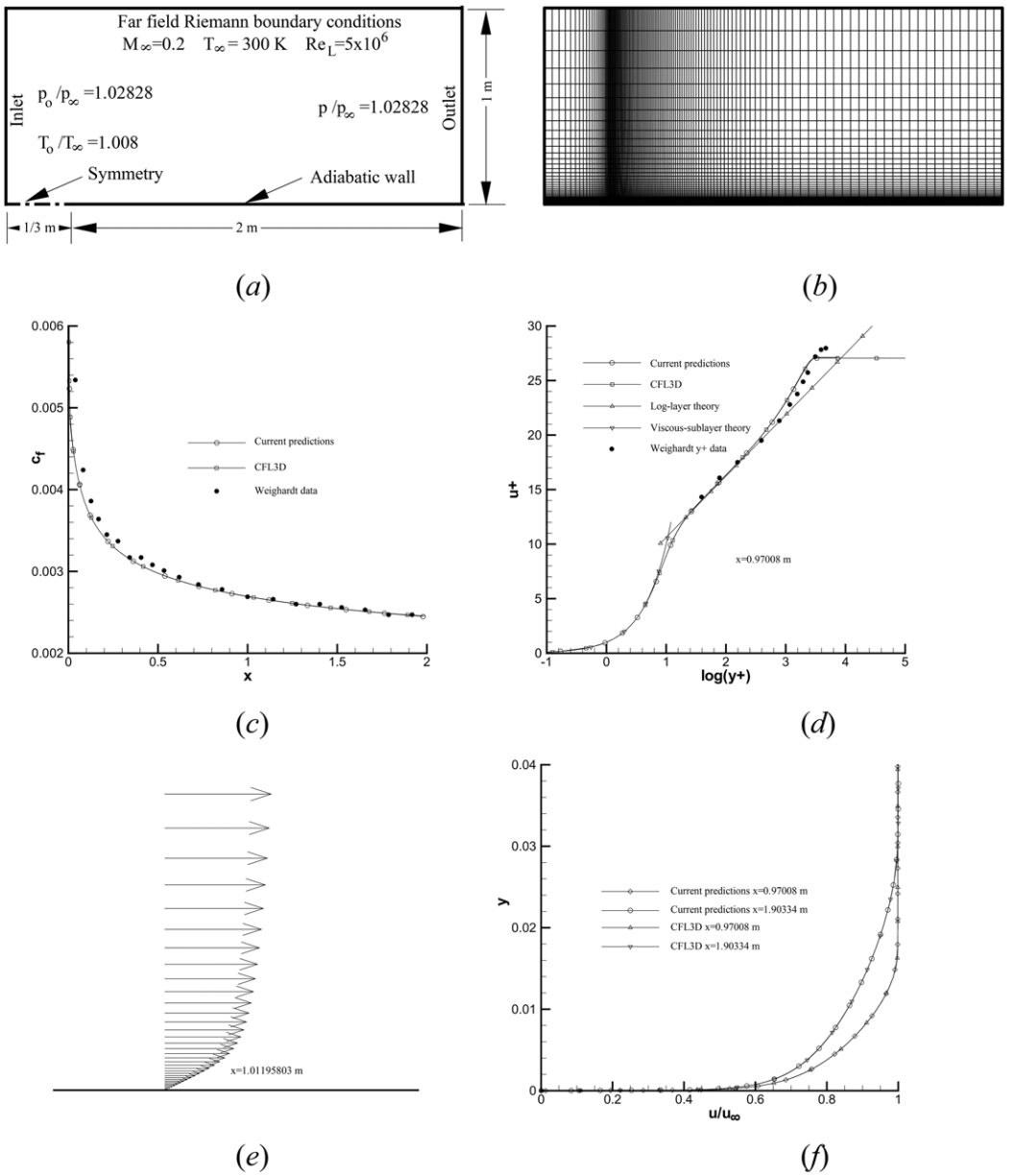

Figure 2. Subsonic turbulent flow over a flat plate; (a) physical situation and boundary conditions; (b) grid system used; (c) comparison of the skin friction coefficient along the plate surface with measurements [46] and numerical results generated using CFL3D [45]; (d) comparison of u + versus y + values at $x = 0.97$ m with measurements [46], theoretical, and numerical values [45]; (e) vector plots showing the velocity profile at $x = 1.012$ m; (f) comparison of velocity profiles at two axial stations with similar profiles obtained using CFL3D [45].

sublayer, with measured data reported by Weighardt [46], and with numerical density-based predictions published in [45]. As shown pressure-based and density-based profiles are on top of each other and very close to measured values. Figure 2*e* shows vector plots of the velocity profile near the plate surface. The linear variation of velocity in the viscous sub-layer is clear. Finally, the generated velocity profiles at two axial stations are compared with similar ones generated using CFL3D [45] in Figure 2*f*. As shown, excellent agreement is obtained. Results demonstrate the correctness of implementation of the pressure far field boundary condition.

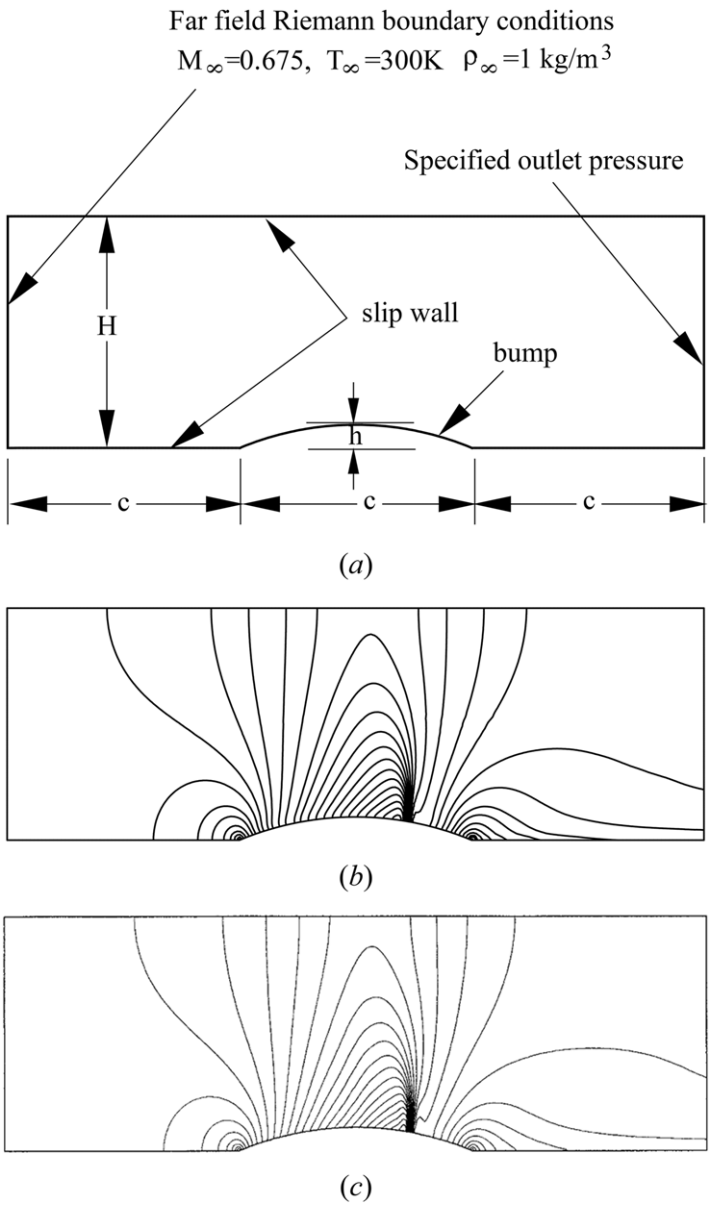

Figure 3. Transonic inviscid flow over a circular arc bump in a channel; (a) physical situation and boundary conditions; (b) Mach contours generated using the proposed methodology; (c) Mach contours reported by Demirdzic et al. [22].

5.2. Case 2: Inviscid transonic flow over a circular arc bump

To test their numerical methods, workers have used this well-known configuration extensively (e.g. [22, 27]). A schematic of the physical domain showing the applied boundary conditions is depicted in Figure 3*a*. The width of the channel (H) is equal to the length of the circular arc bump (c). The maximum height of the bump is $h/c = 0.1$. The flow is treated as inviscid and the slip condition is enforced on all walls. The pressure far field boundary condition is applied at inlet to the domain. With a free stream Mach number value of 0.675, the flow becomes supersonic over the bump, passes through a shock wave and exits as subsonic.

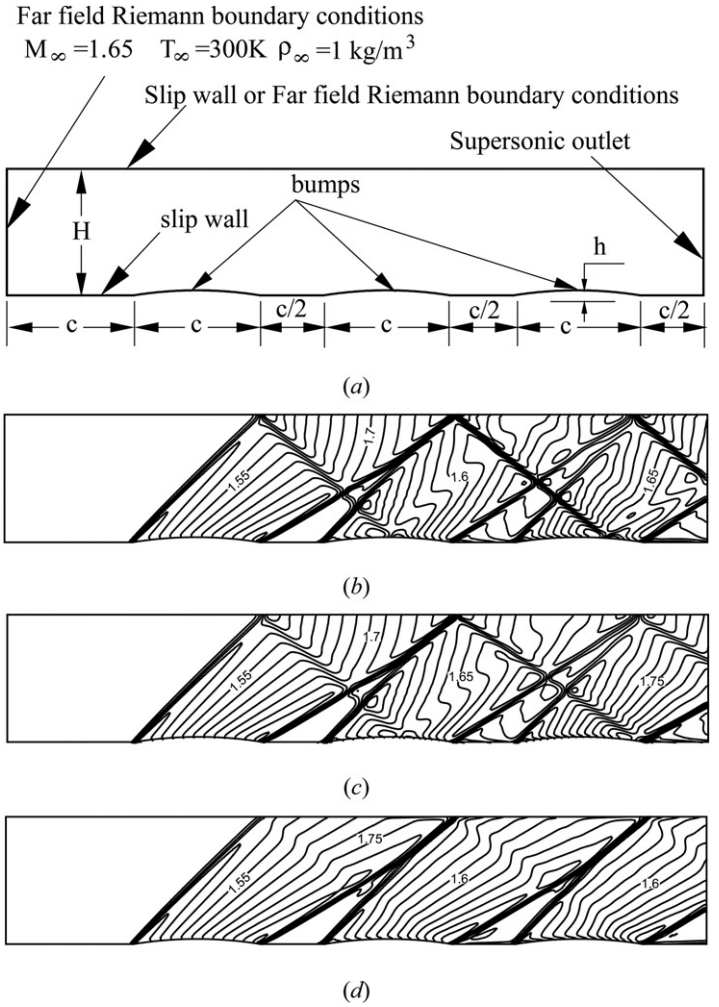

Figure 4. Supersonic inviscid flow over three circular arc bumps in a channel; (a) physical situation and boundary conditions; (b) Mach contours generated by applying a slip wall boundary condition on the upper horizontal boundary; (c) Mach contours generated by applying a specified pressure boundary condition on the upper horizontal boundary; (d) Mach contours generated by applying a pressure far field boundary condition on the upper horizontal boundary.

Mach number contours over the domain generated by the current pressure-based solver with a pressure far field boundary condition applied at inlet and displayed in Figure 3*b* are seen to be in excellent agreement with similar contours reported by Demirdzic et al. [22] and presented in Figure 3*c*. This is another demonstration of the validity of the newly developed treatment of the pressure far field boundary condition.

5.3. Case 3: Inviscid supersonic flow over three equidistant circular arc bumps

This configuration schematically depicted in Figure 4*a* is geometrically similar to the previous one except that $h/c = 0.04$ and three circular arc bumps placed in series are used. Again, the pressure far field boundary condition is applied at inlet to the domain. However, the free stream Mach number is set to 1.65, leading to a supersonic flow in the computational domain. The flow is treated as inviscid and the slip condition is applied on walls. The problem is solved for the

case when the upper horizontal boundary is treated as a slip wall and the case when it is treated as a far field boundary. In the latter case, two boundary conditions are applied for comparison; namely, a specified static pressure and a pressure far field.

Mach contours over the domain for the different boundary conditions are presented in Figures 4*b*–4*d*. For the slip wall boundary condition on the upper horizontal boundary, results are depicted in Figure 4*b*. The reflections of the oblique shock waves at the upper wall and their interaction with the shock waves emanating from the lower wall are easily seen in the plot. For the case when a static pressure boundary condition is applied on the upper horizontal boundary, the shock structure over the domain shown in Figure 4*c* is very similar to that obtained with a slip wall condition, indicating high reflection at that boundary. This wave reflection into the domain is highly reduced with the pressure far field boundary condition (Figure 4*d*). This reflection could be eliminated by applying the pressure far field condition farther away from the wall, as demonstrated next.

5.4. Case 4: Turbulent flow over an axisymmetric transonic bump

In this test case schematically depicted in Figure 5a, axisymmetric geometry is considered. Unlike the previous two configurations, the flow over the bump is treated as turbulent. The lower horizontal boundary and bump are treated as adiabatic no slip walls. The remaining boundaries are modeled as pressure far field boundary conditions as they are applied far away from any influence of the bump. The problem is solved for a free stream Mach number, temperature, and Reynolds number of values 0.875, 300 K, and 2.763×10^6, respectively. The Reynolds number is computed based on a chord of unit length. Isobars and Mach contours over the domain are depicted in Figures 5b, c, respectively. The transonic nature of the flow can be inferred easily from the plots, which show the shock wave formation over the bump. Because the pressure far field boundary condition is applied far away from the bump, no wave reflection into the domain occurs.

Figure 6 depicts comparisons of current results with experimental data [47] and similar numerical results generated using CFL3D [45]. The pressure coefficient over the bump is displayed in Figure 6a. As shown current and CFL3D numerical results are in good agreement and close to measurements. The difference between numerical results and experimental data is attributed to the Spalart-Allmaras turbulence model used. The variations in the skin friction coefficient reported in Figure 6b indicate that current predictions are in excellent agreement with values obtained using CFL3D [45]. This is equally true for the velocity profiles at different axial locations reported in Figure 6c, with y' representing the local distance from the wall. Numerical results are in very good agreement and are very close to measured values. Finally, the streamlines plotted in Figure 6d clearly show the separation region at the trailing edge of the bump. Once more, results generated demonstrate the correctness of the suggested treatment for the pressure far field boundary condition.

5.5. Case 5: Turbulent flow over a NACA 0012 airfoil at 10° angle of attach

The physical situation and boundary conditions for this test case are depicted in Figure 7*a*. The far field boundary is placed at a distance of 500 chords around the airfoil. The no-slip boundary condition is applied on the adiabatic airfoil surface while the pressure far field boundary condition is applied on the far field boundary. The turbulent flow problem is solved for a free stream Mach number, static temperature, and Reynolds number per unit chord (c) with values of 0.15, 300 K, and 6×10^6, respectively. The flow approaches the airfoil at an angle of attack $\alpha = 10^{\circ}$. Figure 7*b* depicts the streamlines around the leading edge of the airfoil and clearly shows the location of the stagnation point on its lower surface. Comparisons of current predictions with

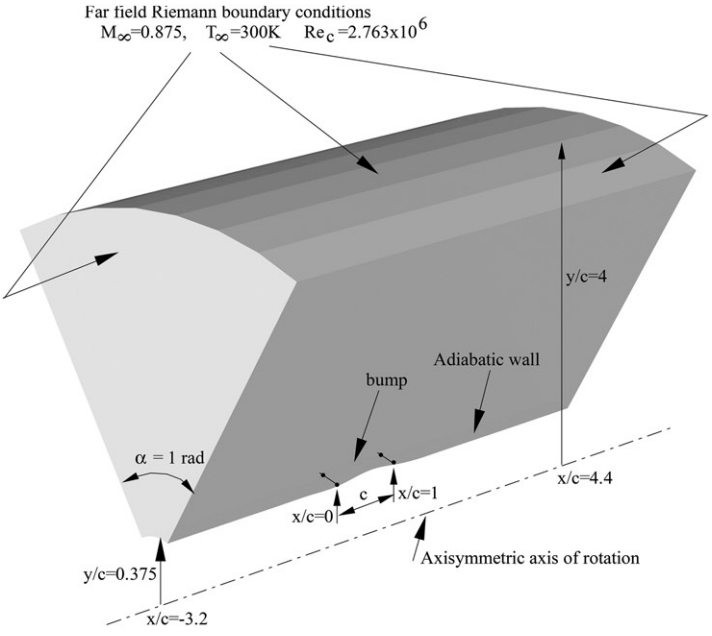

(a)

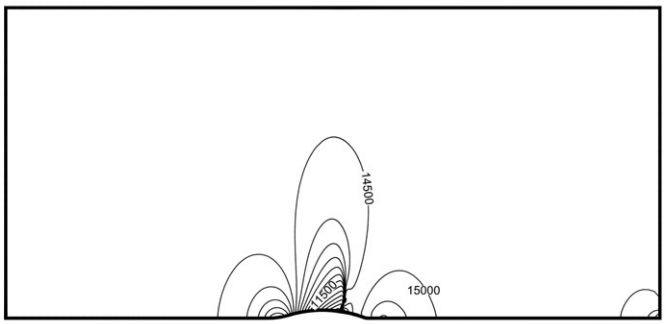

(b)

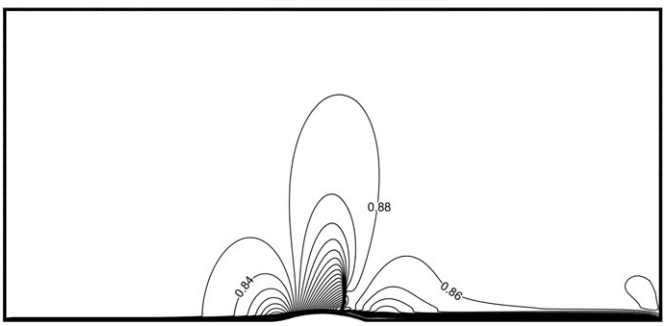

(c)

Figure 5. Transonic turbulent flow over an axisymmetric bump; (a) physical situation and boundary conditions; (b) isobars over the domain; (c) Mach contours over the domain.

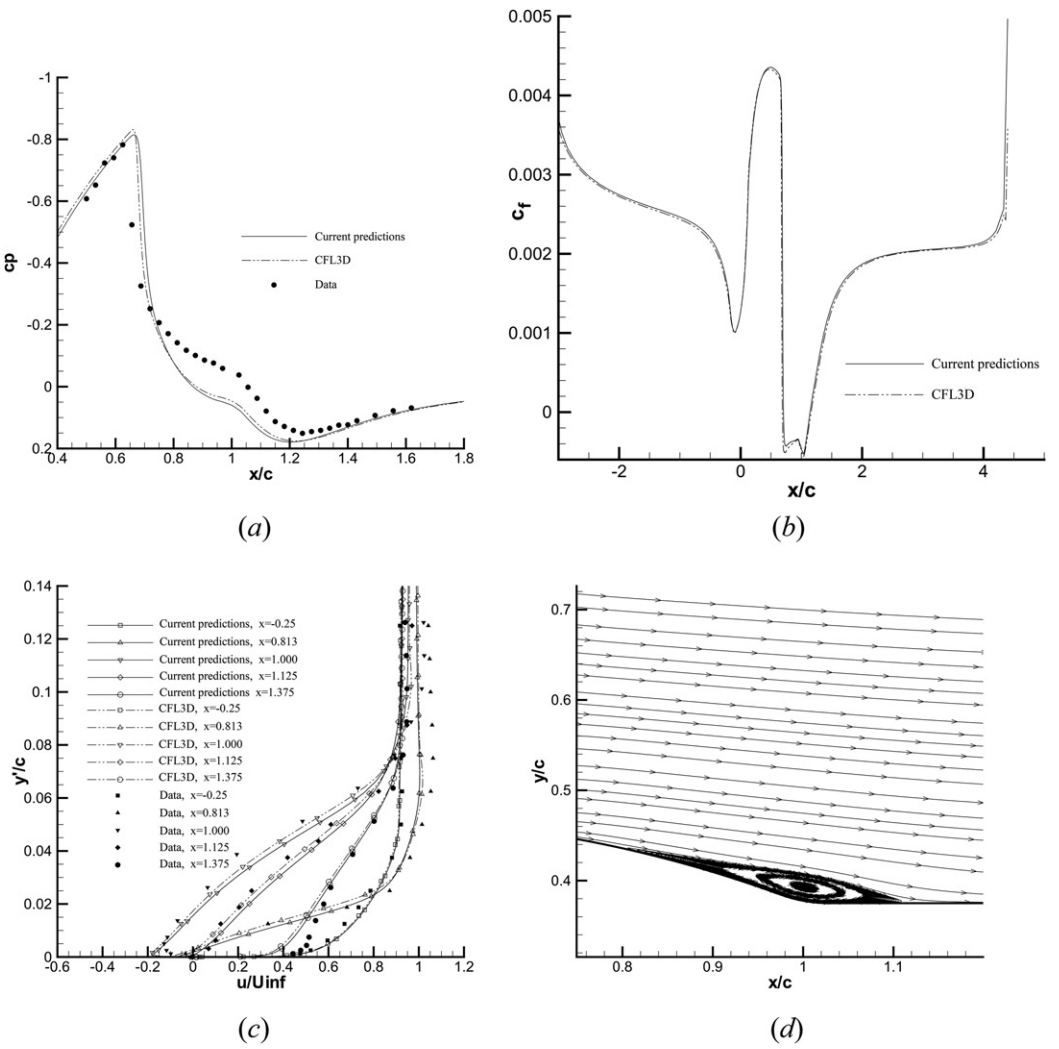

Figure 6. Comparison for the transonic turbulent flow over an axisymmetric bump of (a) the pressure coefficient over the bump surface, (b) the skin friction coefficient over the entire wall, and (c) the velocity profiles at several axial locations with experimental data [47] and/or similar numerical results generated using the CFL3D code [45]; (d) streamlines showing the recirculation region at the bump trailing edge.

similar numerical results reported in [45] and the experimental data of Gregory and O'reilly [48] are displayed in Figures 7*c*, *d*. As shown, numerical predictions of the pressure coefficient c_p (Figure 7*c*) and the skin-friction coefficient c_f (Figure 7*d*) are on top of each other and the pressure coefficient over the upper surface of the airfoil (Figure 7*c*) is in excellent agreement with measurements. Results demonstrate one more time the correct implementation in a pressure-based solver of the pressure far field boundary condition.

5.6. Case 6: Turbulent flow over the three-dimensional ONERA M6 wing at 3.06° angle of attach

Figure 8*a* depicts the physical situation and boundary conditions for this test case. In order to reduce the size of the three-dimensional computational grid, the far field boundary is placed at a

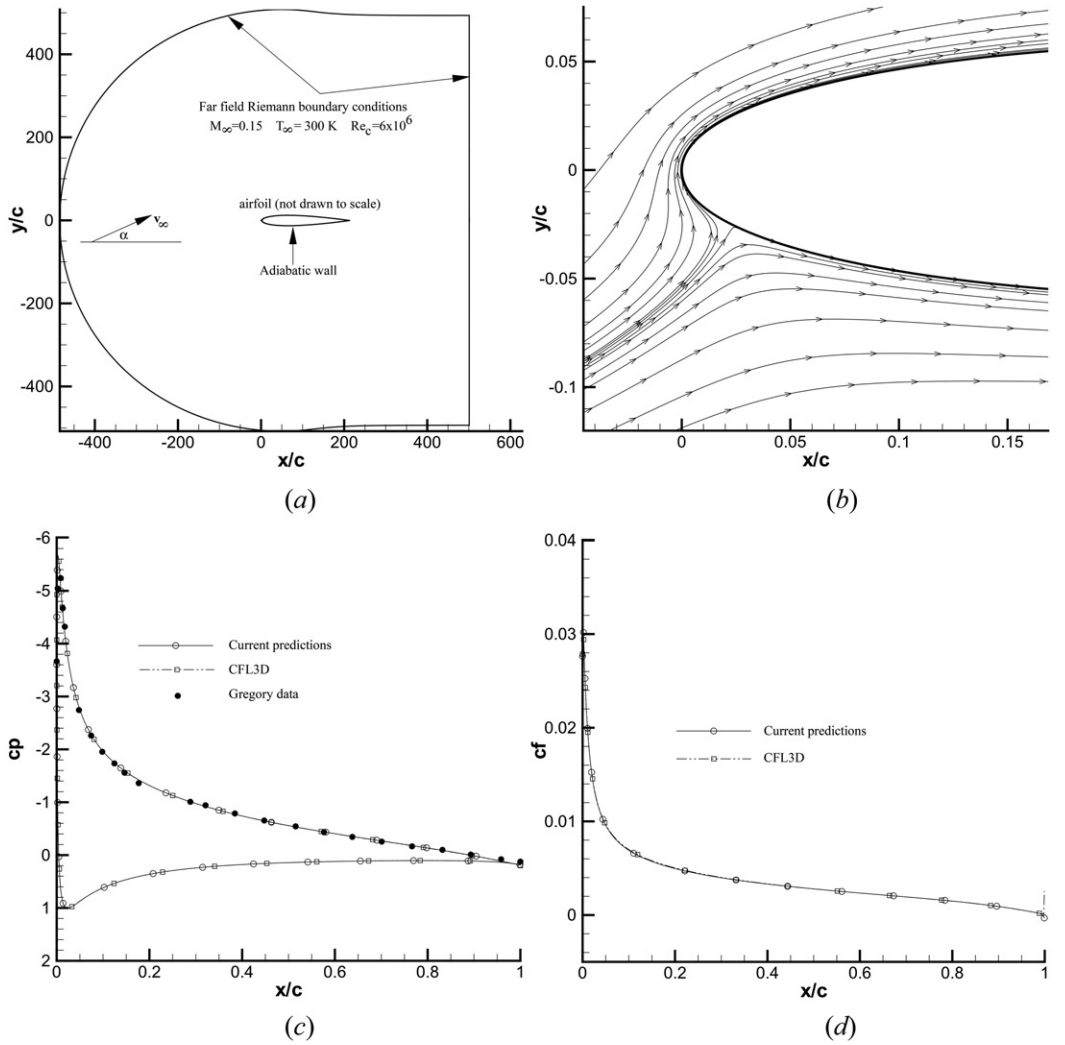

Figure 7. Turbulent flow over an NACA0012 airfoil at 10° angle of attack; (a) physical situation and boundary conditions; (b) streamlines around the airfoil leading edge; (c) comparison of predicted pressure coefficient values over the airfoil with experimental data [48] and similar ones generated using the CFL3D code [45]; (d) comparison of predicted skin friction coefficient values over the upper surface of the airfoil with similar ones generated using the CFL3D code [45].

distance of only 10 chords around the wing. This may slightly affect the accuracy of predictions. The no-slip boundary condition is applied on the adiabatic wing surface; the slip boundary condition is enforced on the vertical plane, while the pressure far field boundary condition is imposed on the far field boundary. The turbulent flow problem is solved for a free stream Mach number, static temperature, and Reynolds number per unit chord (c) with values of 0.84, 300 K, and 14.6×10^6, respectively. The flow approaches the wing at an angle of attack $\alpha = 3.06^{\circ}$. Pressure contours on the surface of the wing and the symmetry plane are displayed in Figure 8*b*. These contours are in excellent agreement with similar ones reported in [45] and clearly show the transonic nature of the flow as revealed by the weak shock wave developing over the wing. Comparisons of current predictions with the experimental data of Schmidtt and Charpin [49] are displayed in Figures 8*c* and *d*. As shown, numerical predictions of the pressure coefficient c_p over the wing surface at $y/b = 0.2$ (Figure 8*c*) and $y/b = 0.44$ (Figure 8*d*) are in good agreement with

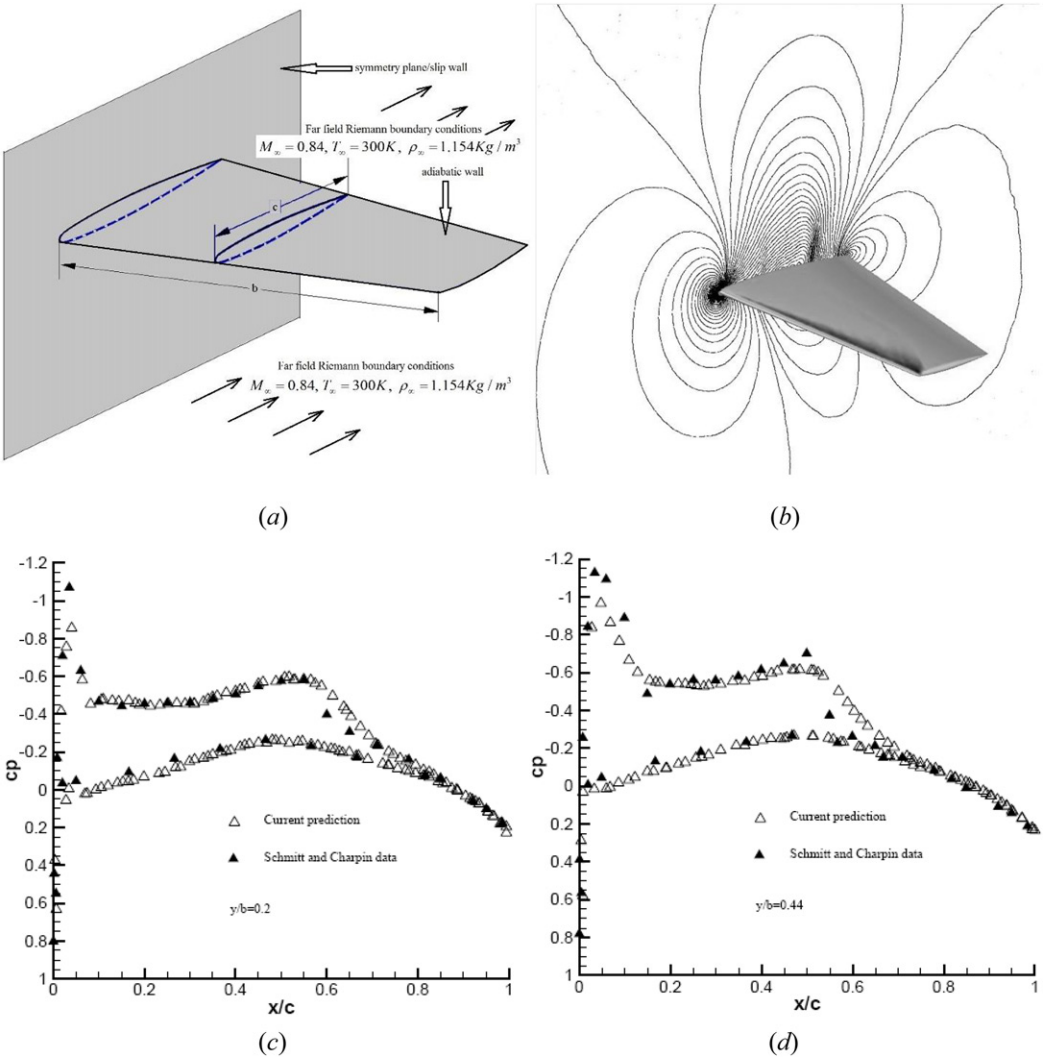

Figure 8. Turbulent flow over the ONERA M6 wing at 3.06° angle of attack; (a) physical situation and boundary conditions; (b) pressure contours on the surface and symmetry plane of the wing; comparison of predicted pressure coefficient values with experimental data [49] on the wing surface at (c) $y/b = 0.2$ and (d) $y/b = 0.44$.

measurements. Again, results demonstrate the correct implementation in a pressure-based solver of the pressure far field boundary condition.

6. Closing remarks

The pressure far field boundary condition was implemented in a pressure-based solver in the context of the finite volume method. The method was tested by solving several inviscid and turbulent flow problems in the subsonic, transonic, and supersonic regimes. Predictions were compared with experimental data and similar numerical predictions obtained using a density-based method and found to be in excellent agreement.

Acknowledgments

Computations were performed at the American University of Beirut.

References

[1] A. Jameson, "Solution of the Euler Equations For Two Dimensional Transonic Flow by a Multigrid Method," *Appl. Math. Comput.*, vol. 13, no. 3-4, pp. 327–356, 1983. DOI: 10.1016/0096-3003(83)90019-X.

[2] A. Jameson, W. Schmidt, and E. Turkel, "Numerical Solution of the Euler Equations by Finite Volume Methods Using Runge-Kutta Time Stepping Schemes," AIAA 14th Fluids and Plasma Dynamic Conference, Paper 81-1259, Palo Alto, California, June 23–25, 1981.

[3] A. Jameson, and T. J. Baker, "Solution of the Euler Equations for Complex Configurations". Proc. 6th AIAA Computational Fluid Dynamics Conference," AIAA Paper, pp. 293–302, 1983. 83-1929, Danvers, July

[4] M. J. Berger, and A. Jameson, "Automatic Adaptive Grid Refinement for the Euler Equations". *AIAA J.*, vol. 23, no. 4, pp. 561–568, 1985. DOI: 10.2514/3.8951.

[5] A. Jameson, and S. Wolfgang, "Some Recent Developments in Numerical Methods for Transonic Flows," *Computer Methods Appl. Mech. Eng.*, vol. 51, no. 1-3, pp. 467–493, 1985. DOI: 10.1016/0045-7825(85)90043-X.

[6] A. Rizzi, and L. E. Eriksson, "Computation of inviscid incompressible flow with rotation," *J. Fluid Mech.*, vol. 153, no. 1, pp. 275–312, 1985. DOI: 10.1017/S0022112085001264.

[7] D. Choi, and C. L. Merkle, "Application of time-iterative schemes to incompressible flow," *AIAA J.*, vol. 23, no. 10, pp. 1518–1524, 1985. DOI: 10.2514/3.9119.

[8] Y. H. Choi, and C. L. Merkle, "The application of preconditioning to viscous flows," *Comput. Phys.*, vol. 105, no. 2, pp. 207–223, 1993. DOI: 10.1006/jcph.1993.1069.

[9] D. L. Tweedt, R. V. Chima, and E. Turkel, Preconditioning for Numerical Simulation of Low Mach Number Three-Dimensional Viscous Turbomachinary Flows, Technical Paper 97-1828. AIAA Press, Washington, DC, 1997.

[10] J. M. Weiss, and W. A. Simith, "Preconditioning applied to variable and constant density flows," *AIAA J.*, vol. 33, no. 11, pp. 2050–2057, 1995. DOI: 10.2514/3.12946.

[11] C. L. Merkle, J. Y. Sullivan, P. E. O. Buelow, and S. Venkateswaran, "Computation of flows with arbitrary equations of state," *AIAA J.*, vol. 36, no. 4, pp. 515–521, 1998. DOI: 10.2514/2.424.

[12] J. R. Edwards, and M. S. Liou, "Low-diffusion flux-splitting methods for flows at all speeds," *AIAA J.*, vol. 36, no. 9, pp. 1610–1617, 1998. DOI: 10.2514/2.587.

[13] S. V. Patankar, and D. B. Spalding, "A calculation procedure for heat, mass and momentum transfer in three-dimensional parabolic flows," *Int. J. Heat Mass Transf.*, vol. 15, no. 10, pp. 1787–1806, 1972. DOI: 10.1016/0017-9310(72)90054-3.

[14] J. P. Van Doormaal, and G. D. Raithby, "Enhancement of the SIMPLE method for predicting incompressible fluid flows," *Numer. Heat Transfer*, vol. 7, pp, pp. 147–163, 1984. DOI: 10.1080/01495728408961817.

[15] S. Acharya, and F. Moukalled, "Improvements to incompressible flow calculation on a non-staggered curvilinear grid," *Numer. Heat Transfer, Part B Fundam.*, vol. 15, pp, pp. 131–152, 1989. DOI: 10.1080/10407798908944897.

[16] S. V. Patankar, *Numerical Heat Transfer and Fluid Flow*. New York, Hemisphere Publishing Corporation, 1980.

[17] A. Ashrafizadeh, B. Alinia, and P. Mayeli, "A New Co-Located Pressure-Based Discretization Method for the Numerical Solution of Incompressible Navier-Stokes Equations," *Numer. Heat Transfer, Part B Fundam.*, vol. 67, no. 6, pp. 563–589, 2015. DOI: 10.1080/10407790.2014.992094.

[18] M. Darwish, A. Abdel Aziz, and F. Moukalled, "A Coupled Pressure-Based Finite-Volume Solver for Incompressible Two-Phase Flow," *Numer. Heat Transfer, Part B Fundam.*, vol. 67, no. 1, pp. 47–74, 2015. DOI: 10.1080/10407790.2014.949500.

[19] F. Moukalled, L. Mangani, and M. Darwish, *The Finite Volume Method in Computational Fluid Dynamics: An Advanced Introduction with OpenFOAM® and Matlab®*. Cham: Springer International Publishing, 2015.

[20] K. C. Karki, A calculation procedure for viscous flows at all speeds in complex geometries, Ph.D. thesis (University of Minnesota, 1986).

[21] C. H. Marchi, and C. R. Maliska, "A non-orthogonal finite-volume methods for the solution of all speed flows using co-located variables," *Numer. Heat Transfer, Part B Fundam.*, vol. 26, no. 3, pp. 293–311, 1994. DOI: 10.1080/10407799408914931.

[22] I. Demirdzic, Z. Lilek, and M. Peric, "A Collocated finite volume method for predicting flows at all speeds," *Int. J. Numer. Methods Fluids*, vol. 16, pp. 1029–1050, 1993. DOI: 10.1002/fld.1650161202.

[23] F. Moukalled, and M. Darwish, "A unified formulation of the segregated class of algorithms for fluid flow at all speeds," *Numer. Heat Transfer, Part B Fundam.*, vol. 37, no. 1, pp. 103–139, 2000. DOI: 10.1080/104077900275576.

[24] A. Nouri-Borujerdi, and A. S. Ghazani, "A pressure-based algorithm for internal compressible turbulent flows through a geometrical singularity," *Numer. Heat Transfer, Part B Fundam.*, vol. 72, no. 1, pp. 82–107, 2017. DOI: 10.1080/10407790.2019.1612665.

[25] I. Sezai, "Implementation of boundary conditions in pressure-based finite volume methods on unstructured grids," *Numer. Heat Transfer, Part B Fundam.*, vol. 75, no. 2, pp. 127–143, 2019. DOI: 10.1080/10407790.2017.1338077.
[26] H. Tan, "Applying the free-slip boundary condition with an adaptive cartesian cut-cell method for complex geometries," *Numer. Heat Transfer, Part B Fundam.*, vol. 74, no. 4, pp. 661–684, 2018. DOI: 10.1080/10407790.2018.1562770.
[27] F. Moukalled, L. Mangani, and M. Darwish, "Implementation of boundary conditions in the finite volume pressure-based method-part I: segregated solvers," *Numer. Heat Transfer, Part B Fundam.*, vol. 69, no. 6, pp. 534–562, 2016. DOI: 10.1080/10407790.2016.1138748.
[28] Pulliam, T. "Characteristic Boundary Conditions for the Euler Equations," Proceeding of Symposium on Numerical Boundary Condition Procedures NASA CP–2201, pp. 165–181, 1981.
[29] J. Carlson, "Inflow/Outflow Boundary Conditions with Application to FUN3D," NASA/TM-2011-217181, 2011.
[30] A. Jameson, and D. Mavriplis, "Finite Volume Solution of the Two-Dimensional Euler Equations on a Regular Triangular Mesh," AIAA 23rd Aerospace Sciences Meeting, Reno, Nevada, January 14–17, AIAA-85-0435, 1985.
[31] S. R. Mathur, and J. Y. Murthy, "All Speed Flows on Unstructured Meshes Using a Pressure Correction Approach," AIAA 14th Computational Fluid Dynamics Conference-Norfolk, VA. USA, November 1–5, 1999 (paper # AIAA-99-3365).
[32] P. R. Spalart, and S. R. Allmaras, "A One-Equation Turbulence Model for Aerodynamic Flows," *Recherche Aerospatiale*, no. 1, pp. 5–21, 1994.
[33] P. R. Spalart, "Trends in Turbulence Treatments," Fluids 2000 Conference and Exhibit, paper no. AIAA 2000-2306, June 2000.
[34] P. R. Spalart, and C. L. Rumsey, "Effective inflow conditions for turbulence models in aerodynamic calculations," *AIAA J.*, vol. 45, no. 10, pp. 2544–2553, 2007. DOI: 10.2514/1.29373.
[35] I. Demirdzic, A Finite Volume Method for Computation of Fluid Flow in Complex Geometries, Ph.D. Thesis, University of London, 1982.
[36] S. Muzaferija, Adaptive Finite Volume Method for Flow Predictions Using Unstructured Meshes and Multigrid Approach, Ph.D. thesis, University of London, 1994.
[37] I. Demirdzic, and S. Musaferija, "Numerical method for coupled fluid flow, heat transfer and stress analysis using unstructured moving meshes with cells of arbitrary topology," *Comput. Methods Appl. Mech. Eng.*, vol. 125, pp. 235–255, 1995.
[38] S. R. Mathur, and J. Y. Murthy, "A pressure-based method for unstructured meshes," *Numer. Heat Transfer, Part B Fundam.*, vol. 31, no. 2, pp. 195–215, 1997. DOI: 10.1080/10407799708915105.
[39] H. Jasak, Error Analysis and Estimation for the Finite Volume Method with Applications to Fluid Flow, PhD. thesis, Imperial College, London, 1996.
[40] I. Demirdzic, "On the discretization of the diffusion term in finite-volume continuum mechanics," *Numer. Heat Transfer, Part B Fundam.*, vol. 68, no. 1, pp. 1–10, 2015.
[41] B. P. Leonard, "Locally modified quick scheme for highly convective 2-D and 3-D flows," in *Numerical Methods in Laminar and Turbulent Flows*, vol. 5, C. Taylor and K. Morgan, (Eds.). Swansea, U.K.: Pineridge Press, 1987, pp. 35–47.
[42] S. G. Rubin, and P. K. Khosla, "Polynomial interpolation method for viscous flow calculations," *J. Comput. Phys.*, vol. 27, pp. 153–168, 1982.
[43] F. Moukalled, and M. Darwish, "Transient schemes for capturing interfaces of free-surface flows," *Numer. Heat Transfer, Part B Fundam.*, vol. 61, no. 3, pp. 171–203, 2012. DOI: 10.1080/10407790.2012.666145.
[44] C. M. Rhie, and W. L. Chow, "A numerical study of the turbulent flow past an isolated airfoil with trailing edge separation," *AIAA J.*, vol. 21, no. 11, pp. 1525–1532, 1983. DOI: 10.2514/3.8284.
[45] Turbulence Modeling Resource. Available: https://turbmodels.larc.nasa.gov/index.html
[46] K. Wieghardt, and W. Tillman, "On the turbulent friction layer for rising pressure," NACA TM-1314, 1951.
[47] W. D. Bachalo, and D. A. Johnson, "Transonic, turbulent boundary-layer separation generated on an axisymmetric flow model," *AIAA J.*, vol. 24, no. 3, pp. 437–443, 1986. DOI: 10.2514/3.9286.
[48] N. Gregory, and C. L. O'reilly, " Low-Speed Aerodynamic Characteristics of NACA 0012 Aerofoil Section, including the Effects of Upper-Surface Roughness Simulating Hoar Frost," Aeronautical Research Council, Aerodynamics Division N.P.L., Reports and Memoranda No. 3726, London, January, 1970.
[49] V. Schmitt, and F. Charpin, "Pressure Distributions on the ONERA-M6-Wing at Transonic Mach Numbers," *Experimental Data Base for Computer Program Assessment*. Report of the Fluid Dynamics Panel Working Group 04, AGARD AR 138, May 1979.